Research Article | Vol. 32, No. 26 / 16 Dec 2024 / Optics Express 46225
Optics EXPRESS

In-plane beam focusing via integrated photonic gradient-index subwavelength grating metalens

Nafiz Jaidye,[1] Jaewhan Lee,[2] Daniel Pimbi,[3] Myoung-Hwan Kim,[1] Ayrton Bernussi,[3] and Sangsik Kim[1,2,3,4,*]

[1]Department of Physics and Astronomy, Texas Tech University, Lubbock, Texas 79409, USA
[2]Graduate School of Quantum Science and Technology, Korea Advanced Institute of Science and Technology, Daejeon 34141, Republic of Korea
[3]Department of Electrical and Computer Engineering, Texas Tech University, Lubbock, Texas 79409, USA
[4]School of Electrical Engineering, Korea Advanced Institute of Science and Technology, Daejeon 34141, Republic of Korea
*sangsik.kim@kaist.ac.kr

Abstract: We present an in-plane beam converter scheme that can focus a large Gaussian slab mode into a tightly focused spot approximately hundreds of micrometers away from the chip facet. Our approach involves designing the modal expander that converts a photonic waveguide mode to a large Gaussian slab mode and engineering the two-dimensional (2D) gradient-index subwavelength grating arrays that modify modal wavefront to be focused as the beam propagates. The device is designed on a monolithic silicon nitride scheme, which is transparent at the visible wavelength regime and readily available for the complementary metal-oxide-semiconductor process. Our device can be utilized in various chip-scale photonic applications, especially involving biochemical species and target samples ranging from one to tens of micrometer scales.

1. Introduction

Silicon nitride (Si_3N_4) has emerged as a promising material for integrated photonics due to its properties, including a relatively high refractive index, high Kerr nonlinearity, thermal stability, low optical loss at telecommunication wavelengths, and broadband transparency extending into the visible regime. These characteristics make Si_3N_4 an attractive platform for various integrated photonic applications, particularly those involving visible light. Moreover, Si_3N_4 is compatible with well-established complementary metal-oxide-semiconductor (CMOS) processes, enabling mass production and cost-effective solutions for photonic integrated circuits (PICs) [1,2]. Si_3N_4-based PICs have been successfully employed in diverse chip-scale applications, such as atomic physics [3–5], quantum photonics [6–8], time-frequency metrology [9,10], and biochemical sensing [11–13]. As Si_3N_4 PIC technology continues to advance, there is an increasing demand for integrating PICs with other physical domains, including microfluidics [14–19] and atomic vapor cells [20–24]. This integration represents a natural progression towards the next generation of PIC applications, akin to the advancements in various tabletop optical technologies in free-space environments. Ultimately, the goal is to harness optical functionalities in conjunction with other physical systems through light-matter interactions. However, realizing these hybrid systems on a chip scale poses challenges due to mismatched optical mode sizes across different domains. Consequently, the development of efficient modal converters is crucial for bridging this gap and advancing hybrid integrated photonic systems.

In recent years, various approaches have been explored to enable the hybrid integration of photonic integrated circuits (PICs) with other physical domains. One such approach employs an on-chip extreme mode converter to interface and hybridize photonic systems with atomic systems [4,5,25]. The extreme mode converter generates a collimated Gaussian beam with a waist size of

#539591 https://doi.org/10.1364/OE.539591
Journal © 2024 Received 16 Aug 2024; revised 29 Oct 2024; accepted 18 Nov 2024; published 6 Dec 2024

Optics EXPRESS

hundreds of micrometers and a flat wavefront in free space, facilitating chip to free space to chip coupling over a 4 mm propagation distance. This enables the integration of PICs with atomic vapor cells for applications such as laser stabilization [4] and atomic wavelength referencing [5]. However, the need for precise vertical alignment between the photonic chip and the atomic vapor cell chamber presents a challenge to efficient interfacing, making the hybrid system complex and difficult to operate stably.

Optofluidics has also been investigated for optical trapping and manipulation of particles within fluid environments. Typical approaches, including laser beams [26–29], micro-optics [30–32], and metasurfaces [33–35], often rely on bulky setups involving free-space and out-of-plane beam components, hindering practical applications outside the lab. To address this issue, researchers have explored various schemes for integrating photonic and microfluidic systems onto a single chip, such as liquid-core waveguides [36–39]. This scheme exploits a single channel for both guiding light and fluids to manipulate particles and detect biological samples. While promising, this configuration lacks dedicated trapping elements and sometimes requires complex fabrication steps, compromising the device's detection precision and integrability with other chip components.

Another alternative hybrid integration approach is based on evanescent wave trapping [40–45], which offers a potential on-chip solution for manipulating particles within microfluidic channels. This method utilizes the gradient force generated by an evanescent wave near the waveguide to trap and manipulate particles in the fluid. Due to the short decay length of the evanescent field, interactions are confined to the immediate vicinity of the waveguide. This results in a small microfluidic channel volume and may lead to unintended contact between the sample and the waveguide, potentially disrupting the manipulation process. Moreover, the evanescent field trapping mechanism can exhibit low trapping efficiency and stability issues due to the weak gradient trapping force. Additionally, the non-uniform field intensity distribution around the waveguide may cause random particle trapping, posing a challenge for precise and controlled manipulation of particles.

To overcome these challenges and further advance hybrid PIC integration schemes, a unique and innovative approach is required. This solution should be capable of generating an in-plane beam and facilitating large-scale modal size transformation on-chip, ensuring simple integration and exhibiting potential for interfacing with other systems, such as atomic vapor cells and microfluidics. In this paper, we present an in-plane beam converter design on a Si_3N_4-based integrated photonic chip that converts the photonic waveguide mode to an in-plane Gaussian mode and focuses it in free space at hundreds of micrometers away from the chip facet. The device is designed on a 150 nm-thick Si_3N_4 platform with silicon dioxide (SiO_2) top and bottom claddings, targeting operation in the visible wavelength regime. The in-plane beam converter is composed of two stages: the first stage is a modal expander that converts the photonic waveguide mode to a 1D large Gaussian slab mode, and the second stage consists of gradient-index subwavelength grating (SWG) metalens that manipulate the wavefront of the slab mode such that the out-coupled beam is focused hundreds of micrometers away from the chip. The device is designed on a simple monolithic chip. We fabricate the design and experimentally characterize the in-plane beam focusing by imaging the beam at the visible wavelength. The following sections present the device design at each stage, followed by numerical and experimental results. We analyze the out-coupled beam, examining its evolution, focal spot size, and focal distances while discussing the results in their respective sections.

2. Schematics and design

2.1. Overall schematics of the in-plane beam converter

The proposed integrated photonic silicon nitride device acts as an in-plane mode size converter and lens. The operation of the device can be divided into two steps, as illustrated in Fig. 1(a).

Optics EXPRESS

First, the photonic waveguide mode from the PIC's input waveguide is converted to a large slab mode with a Gaussian intensity distribution via a mode expander [25]. Then, in the second stage, the wavefront of the slab mode is transformed using the 2D gradient-index subwavelength grating (SWG) arrays or in-plane metalens. While most metalens works are developed for *out-of-plane* [46], our SWG metalens are designed *in-plane* to manipulate the wavefront of the slab mode. As the beam travels through the 2D SWG arrays, it converges to a spot in the air after exiting the chip facet. In the schematic of Fig. 1(a), the trajectory of beam conversion is illustrated with red arrows and color. In the mode expander, the gap between the waveguide and the slab determines the evanescent coupling strength and is designed such that the expanded beam exhibits a large Gaussian intensity profile. The minimum gap distance is set large enough to ensure that the waveguide and slab mode coupling do not introduce significant phase distortion. This is an important condition to ensure that the converted slab mode exhibits an almost flat wavefront. In the second stage, the 2D SWG arrays behave similarly to a converging lens, utilizing a gradient-index profile following the Gaussian-distributed filling fraction ρ. As the beam passes through this SWG array metalens, the expanded in-plane beam is focused into free space outside of the chip, corresponding to the designed focal distance. The device is designed based on the fundamental transverse electric (TE_0) mode with 150 nm-thick Si_3N_4 and SiO_2 claddings. It operates at a visible wavelength of $\lambda = 700$ nm, where silicon nitride exhibits low loss [6,47]. The refractive indices of Si_3N_4 and SiO_2 layers at this visible operating wavelength are 2.0091 and 1.4554, respectively.

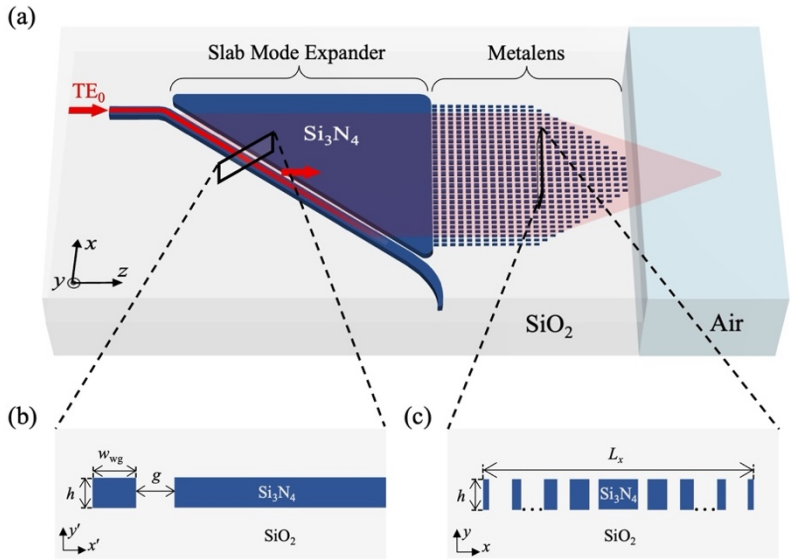

Fig. 1. (a) Schematic diagram of the silicon nitride (Si_3N_4) metalens device with silicon dioxide (SiO_2) claddings. The blue and grey colors represent Si_3N_4 and SiO_2, respectively. The device operation is divided into two steps: (i) Slab mode expander for waveguide to slab mode conversion, and (ii) Subwavelength grating-based metalens for in-plane beam transformation and focusing. The red arrows and color indicate the path of the two-step process. Zoomed-in cross-sections of the (b) Slab mode expander and (c) SWG metalens, where the height $h = 150$ nm, waveguide width $w_{wg} = 350$ nm, gap size g is the gap between the waveguide and the slab and L_x is the length of the metalens structure along the x-axis.

Optics EXPRESS

2.2. Slab mode expander

In large-scale mode conversions, such as those using an inverse-tapered waveguide, there are common issues like wavefront distortion and the need for increased device dimensions for a large mode field variations. To avoid these problems, we used a slab mode expander to convert the waveguide mode to a 1D Gaussian slab mode with a collimated flat wavefront [25]. Engineering the gap profile between the evanescently coupled waveguide and the slab plays a crucial role in the mode conversion process, producing a large Gaussian intensity profile in the slab. Figure 1(b) shows the cross-sectional schematic of the slab mode expander, where the waveguide width is $w_{wg} = 350$ nm. The height of the Si_3N_4 layer is set to $h = 150$ nm and is consistent throughout all components of the device (i.e., waveguide, slab, and gratings).

Figure 2(a) shows the simulated real part of the effective refractive index (n_{eff}) of the waveguide mode as a function of the gap g. The inset shows the field profile of the simulation when the gap is $g = 600$ nm. As the gap increases, the real part of n_{eff} decreases, transitioning from a strong perturbation region to a weak perturbation region. The blue dashed line indicates where the real part of n_{eff} saturates to 1.57055 after $g \approx 600$ nm. Since the real parts of n_{eff} for the waveguide and slab modes are different, the evanescently coupled slab mode from the waveguide propagates with a tilted angle θ_{tilt} with respect to the waveguide direction z'. The tilt angle is determined by $\theta_{tilt} = \cos^{-1}[n_{eff}^{wg}/n_{eff}^{slab}]$, where n_{eff}^{wg} and n_{eff}^{slab} are the real parts of the effective refractive indices of the slab and the waveguide modes, respectively. The simulated slab index is $n_{eff}^{slab} \approx 1.7117$. Therefore, in the weak perturbation region, the tilt angle is approximately $\theta_{tilt} = \cos^{-1}(1.5705/1.7117) \approx 23.43°$.

Figure 2(b) shows the simulated imaginary part of n_{eff} for the waveguide mode (red dots) on a log scale and its exponential fitting curve (black line). Using the exponential fitting curve, we can quantify the coefficients a and b and represent the degree of loss as a function of g, where $\mathrm{Im}(n_{eff}) = ae^{-bg}$. In this case, the coefficients a and $1/b$ are found to be 0.0363 and 84.49422 nm, respectively. To form the Gaussian-intensity distributed slab mode, the gap profile $g(z')$ between the waveguide and the slab is engineered along the waveguide mode propagation direction z', following [25]:

$$g(z') = \frac{1}{b} \ln\left\{\frac{1}{a}\frac{\lambda_0}{\sqrt{2}\pi^{3/2}w}\frac{\exp(-2z'^2/w^2)}{1-\mathrm{erf}(\sqrt{2}z'/w)}\right\}. \quad (1)$$

where λ_0 is the operating wavelength of 700 nm, w is the beam waist along the waveguide propagation direction, and a and b are the fitting coefficients from Fig. 2(b). Since our target beam waist of the slab mode is $w_0 = 100$ µm, considering the tilted beam angle, we set the desired w to be $w = w_0(\sin\theta_{tilt})^{-1} \approx 251.5$ µm. Figure 2(c) shows the calculated gap profile using Eq. (1) along z', spanning from −300 µm to 200 µm. For such a large conversion, the gap profile ideally requires values below 600 nm, resulting in a non-flat wavefront region. Our design has a gap profile below 600 nm, but the phase distortion is not that significant. To assess the degree of wavefront distortion, we plotted the estimated angle at each z' (blue dashed line). The estimated angular distortion is within 0.133 degrees, which would be acceptable for demonstrating the in-plane metalens device presented here. The overall device performance could be improved once the wavefront of this slab mode expander is designed to be entirely flat.

2.3. 2D gradient subwavelength grating metalens

The large slab mode with a Gaussian intensity distribution (beam waist $w_0 = 100$ µm) and a flat wavefront generated in Sec. 2.1 now enters the second stage of beam conversion: the 2D SWG metalens, which consists of the grating array distributions shown in Fig. 1(a). Figure 1(c) illustrates the cross-sectional view of this SWG distribution along the x-axis. The periodicity of each unit cell is fixed to $\Lambda_x = 0.65$ µm while varying the filling fraction $\rho_x^G(x)$ following the

Optics EXPRESS

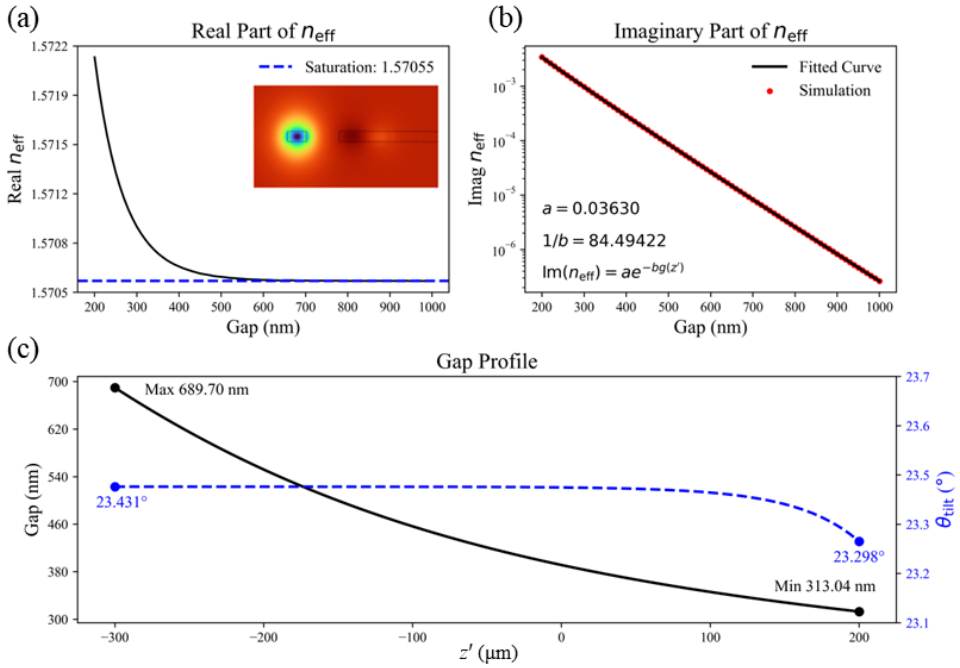

Fig. 2. Simulated effective index (n_{eff}) of the slab-coupled waveguide mode: (a) Real and (b) Imaginary parts. (a) The blue dashed line indicates the saturation value, $\mathrm{Re}(n_{\mathrm{eff}}) = 1.57055$, after g ≈ 600 nm. The inset figure shows the field distributions ($|E|$) at $g = 600$ nm. (b) The red dots represent the simulation results, and the black line is the fitted curve with ae^{-b*g}. The fitting coefficients a and $1/b$ are found to be 0.03630 and 84.49422 (nm), respectively, quantifying the degree of evanescent coupling. (c) The black line indicates the calculated gap profile g, using Eq. (1), along the waveguide spanning from z' = -300 μm to z' = 200 μm. The waveguide height h and width w_{wg} are set to 150 nm and 350 nm, respectively. The blue dashed line shows the tilt angle between the waveguide and the slab modes, following $\theta_{\mathrm{tilt}} = \cos^{-1}[n_{\mathrm{eff}}^{\mathrm{wg}}/n_{\mathrm{eff}}^{\mathrm{slab}}]$. When the gap size is below 600 nm, the angle starts to deviate, but the degree of deviation is less than 0.133 degree.

Gaussian distribution:

$$\rho_x^G(x) = \rho_0 e^{-x^2/2w_{\mathrm{b}}^2} \tag{2}$$

where $\rho_0 = 0.5$. The w_{b} is the SWG metalens width parameter, which is key to controlling the beam transition pattern. At the beginning of the gratings ($z = 0$), w_{b} is set to $w_{\mathrm{b1}} = 220$ μm to support the smooth transition of the entire beam. The physical length of the metalens in the x-direction is defined as L_x and set to 220 μm. Along the beam propagating direction (z-axis), the SWG unit cell period is set to $\Lambda_z = 0.6$ μm while fixing the filling fraction to $\rho_z = 0.5$. Ideally, smaller grating periods are desired to meet the SWG criteria and enhance performance. However, due to fabrication resolution limitations, we utilize larger grating periods. Despite this, our device does not experience significant reflections, likely due to the varying filling fractions, and we refer to our gratings as SWGs, considering the ideal cases. The role of SWG along the z-direction is to expand the beam in the vertical direction, which will prevent the rapid divergence of the out-coupled beam in the y-direction. However, at different z positions, the metalens width parameter w_{b} is linearly reduced from w_{b1} to w_{b2}, where w_{b2} is the metalens width parameter at the end facet. The total length of the SWG metalens along the z-direction is set to L_z, thus the

Optics EXPRESS

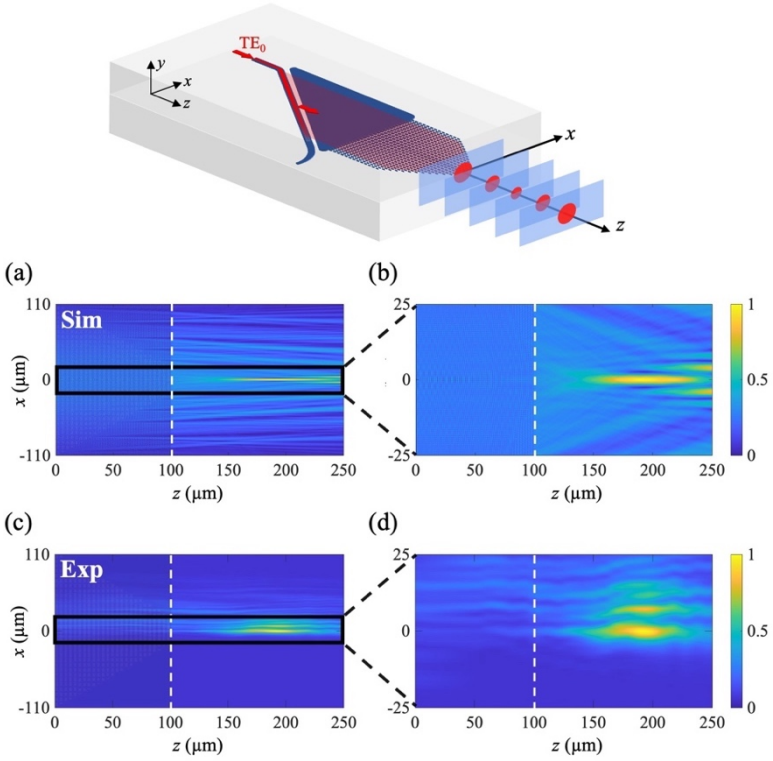

Fig. 3. Simulated and experimentally measured intensity map plots in the xz-plane (top-view) for metalens device with $L_z = 100$ μm, $L_x = 220$ μm and $w_{b2} = 10$ μm. The black solid box indicates the zoomed-in portion of the map plots. The white dashed line represents the facet of the metalens chip. (a) FDTD-simulated field intensity map showing the input beam converging at a focal distance of $f_d \approx 92$ μm. (b) Zoomed-in image of the simulated focal spot. (c) Experimentally characterized intensity map for the same device parameters, demonstrating a focal distance of $f_d \approx 90$ μm. (d) Zoomed-in image of the experimental focal spot. The focal distance f_d is defined as the distance from the chip facet (white dashed line) to the center of the focal spot.

SWG metalens width parameter can be described as the following:

$$w_b(z) = \frac{w_{b1}}{2} - \frac{w_{b1} - w_{b2}}{2L_z} z \tag{3}$$

Note that this $w_b(z)$ variation effectively modifies the filling fraction distribution of the SWG metalens, following Eq. (2). The flat wavefront of the large slab mode input will be varied such that it follows the trajectory of this SWG width parameter variation. This would determine the out-coupled beam trajectory such that the beam converges to a spot away from the chip facet. Since the metalens width parameter is linearly tapered, it acts similarly to a linear cone-shaped axicon, which will generate a Bessel-Gaussian-like focus after leaving the chip.

Figure 3(a) shows the finite-difference time-domain (FDTD) simulation result when the metalens parameters are $L_z = 100$ μm, $L_x = w_{b1} = 220$ μm, and $w_{b2} = 10$ μm. This simulation was performed using a 2.5D FDTD in Ansys Lumerical with a Gaussian slab mode input (TE polarization) and PML boundary conditions. Figure 3(b) is the zoomed-in view of Fig. 3(a), and it clearly shows the beam focusing through the SWG metalens design with a Bessel-Gaussian-like

Optics EXPRESS

extended depth of focus. More details will be discussed in the following section in comparison with the experimental results.

3. Experiment and analysis

3.1. Experimental characterization

The designed chip was fabricated on a monolithic Si_3N_4 film through the LIGENTEC multi-project wafer (MPW) process. The Si_3N_4 layer thickness is 150 nm with 3.3 µm top and 4 µm bottom SiO_2 cladding layers.

Figure 4 shows the chip characterization setup. A single-mode fiber-coupled laser diode source with a constant current driver and temperature controller is used for visible wavelength input at around 700 nm. To set TE_0 mode input polarization, a polarization controller is connected after the laser source. A custom-built edge coupling setup was implemented to stage the chip, and single-mode lensed fiber was used for coupling from the optical fiber to the chip. The out-coupled beam from the chip facet is designed to be in-plane. Therefore, a microscope setup with an objective lens attached to a charge-coupled device (CCD) camera is mounted on an XYZ translation stage for in-plane beam imaging at different locations from the chip facet.

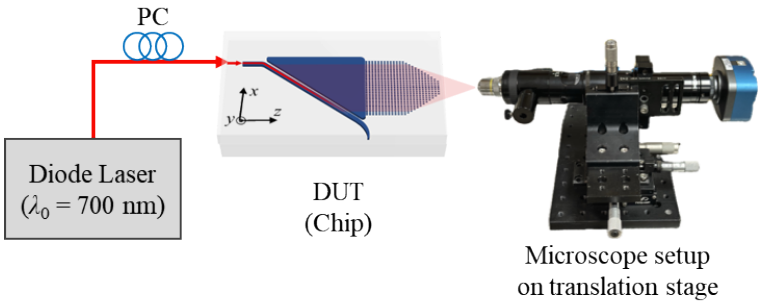

Fig. 4. Experimental setup for in-plane beam characterization. A 700 nm diode laser, coupled with a polarization controller (PC), provides a TE_0-polarized visible wavelength input to the chip or device under test (DUT). The out-coupled in-plane beam is captured using a CCD camera attached to a microscope tube with an objective lens mounted on an XYZ translation stage. The beam images are acquired at different z-positions from the chip edge with 10 µm incremental steps. The red arrow and color indicate the path of the beam as it enters and exits the chip.

The out-coupled beam images were captured in-plane at different z-distances with 10 µm incremental steps. Figures 3(a,b) and 3(c,d) show the simulated and experimental intensity map plots, respectively, in the xz-plane, where z is the propagation direction, and x is the horizontal direction of the chip. The SWG parameters of the in-plane metalens device are $L_z = 100$ µm, $L_x = w_{b1} = 220$ µm, and $w_{b2} = 10$ µm. The white dashed line denotes the chip facet, and the black solid box indicates the zoomed-in view region of the full-scale intensity maps in Figs. 3(b) and 3(d). The Ansys Lumerical finite-difference time-domain (FDTD) module was used for the simulations. The experimental image data were interpolated to generate a two-dimensional (2D) intensity map.

The simulated and experimental full-scale maps in Figs. 3(a) and 3(c) show that the out-coupled beam converges to a spot, especially in the horizontal direction (x-axis). The zoomed-in views illustrated in Figs. 3(b) and 3(d) show this in more detail. The focal distances are approximately $f_d \approx 92$ µm and ≈ 90 µm for simulation and corresponding experimental results, respectively. The focal distance f_d is defined as the distance from the chip facet to the peak of the focal spot.

Optics EXPRESS

Although the out-coupled beam is well-focused on the spot in the x-direction, it is worth noting that the beam exhibits an extended depth of focus in both simulation and experimental results. This can be attributed to the linear variation of the SWG effective index profiles along the beam propagation direction [following Eq. (3) along the z-axis], which causes the Gaussian slab mode to undergo an axicon-like phase variation [48]. Consequently, the out-coupled beam exhibits a Bessel-Gaussian-like beam propagation with an extended depth of focus, as depicted in Fig. 3(b).

The experimental map plots in Figs. 3(c) and 3(d) reveal slightly shifted images toward the positive x-direction, suggesting that the slab mode generated from the modal expander is slightly tilted, while the SWG metalens is designed for normal illumination. This variation also shifts the center position of the input slab mode, resulting in the beam sidelobes being located in the positive x-direction. Nevertheless, the beam focal spot remains in the center position after leaving the chip, and the focal distance closely matches the numerical result, indicating that the off-angle variation is minimal. The measured overall power conversion efficiency from the input fiber to the chip and ultimately to the final beam is approximately -16 dB. This value accounts for all losses from various sources, including input fiber-to-chip coupling, waveguide propagation losses (particularly due to the visible wavelength), slab mode expander, the interface between the slab and gratings, scattering or substrate leakage in the grating region, and reflections at the metalens facet. For characterization, the measurements were conducted in air, but for other applications, such as in water or liquid environments, the coupling efficiency is expected to improve due to the lower index contrast at the interface. Additionally, further optimization of each segment and implementing a thicker cladding would increase the overall coupling efficiency.

More precise and iterative calibration would be required for a more rigorous demonstration to account for fabrication imperfections in the process. Moreover, the beam transition can also be improved by further decreasing the periodicities ($\Lambda << \lambda$) in both x- and z-directions such that the photonic SWGs form an ideal effective medium [49–57]. The diffractions can also be further minimized by optimizing the beam transition pattern, for example, by using an adiabatic smooth variation of the filling fraction in the z-direction instead of the current linearly decreasing function in Eq. (3).

3.2. Out-coupled beam analysis

Figure 5(a) presents the experimentally captured cross-sectional images of the out-coupled beam at different propagation distances (z-positions) from the chip facet. The z-positions labeled A to E represent the microscopic images captured at positions ranging from 50 µm to 130 µm from the chip facet, with a step size of 20 µm. To examine the focusing behavior of the out-coupled beam, Fig. 5(b) plots the peak intensity of each image at the center position as a function of the propagation distance z. The blue dashed-circle line represents the experimentally characterized result, while the orange solid line depicts the corresponding simulation result. Both experimental and simulation results exhibit a close match, confirming the in-plane focusing of the beam to a spot after exiting the metalens chip at $z \approx 190$ µm.

The out-coupled beam intensity reaches its peak at point C ($z \approx 190$ µm) for the experimental data and decreases as the distance from the focus increases. The simulation data follows a similar trend, with the peak intensity position occurring near $z \approx 192$ µm. Since the focal distance is defined as the distance between the metalens facet and the peak intensity position, the simulated and experimental focal distances are comparable and estimated to be $f_{\mathrm{d}} \approx 92$ µm and $f_{\mathrm{d}} \approx 90$ µm, respectively. The slight mismatch between the simulated and experimental intensity values along the propagation distance could be attributed to several factors, such as the tilted expander incident slab mode, positioning uncertainty, and power fluctuations between each z-scanning measurement. These factors may introduce minor discrepancies between the experimental and simulated results. Nevertheless, the overall focusing behavior of the out-coupled beam remains

Optics EXPRESS

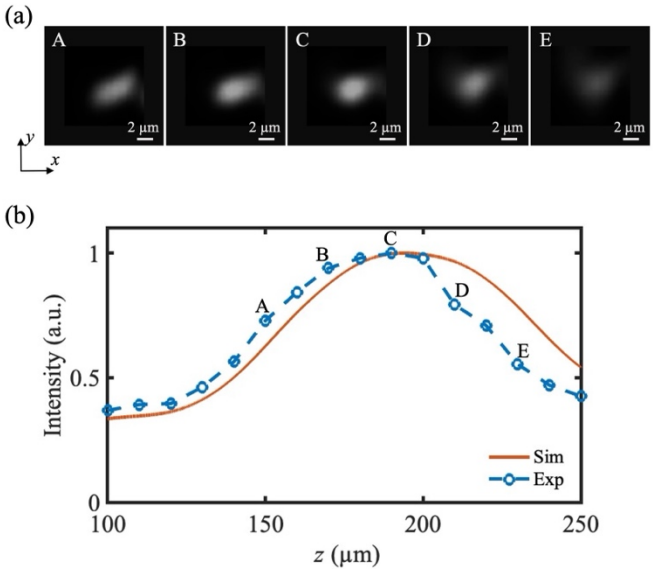

Fig. 5. Evolution of the beam spot after the beam exits the metalens device at $z = 100$ μm. (a) Microscopic in-plane experimental images of the isolated beam spots at position A ($z = 150$ μm), B ($z = 170$ μm), C ($z = 190$ μm), D ($z = 210$ μm) and E ($z = 230$ μm). (b) Simulated (solid orange) and the experimental (dashed blue) intensity plots showing the variation of beam intensity as a function of propagation distance z. The focal spot is observed at position C, corresponding to $z \approx 190$ μm ($f_d \approx 90$ μm since the chip facet is located at $z = 100$ μm).

consistent between the experimental and simulation data, validating the functionality of the in-plane metalens design.

The propagated beam is expected to have the maximum intensity and minimum spot size at the focal spot. In Fig. 5, we identified the focal spot at position C ($z = 190$ μm) by examining the intensity maximum. To quantify the spot size at this focal spot, we replotted the zoomed-in microscopic image at position C in Fig. 6(a). The field intensity distributions along the x- and y-axes are also plotted in Figs. 6(b) and 6(c), respectively. The blue dashed lines represent the experimental data, while the solid orange lines are the Gaussian fitting curves. The intensity distributions along both axes fit well with the Gaussian curves, allowing us to determine the full width at half maximum (FWHM) and beam waist w_0. The beam waist w_0 along the x- and y-axes are approximately 5.87 μm and 3.42 μm, respectively. It is worth noting that the beam waist of the input slab mode is $w_0 = 100$ μm, which has been significantly reduced to ≈ 5.87 μm at the focal spot. This confirms the extreme modal size transformation in the horizontal direction achieved through the in-plane SWG metalens.

Along the vertical direction (y-axis), we used SWG to expand the beam size in the y-direction such that it is large enough to achieve a beam Rayleigh range within ≈ 1.0 mm. To confirm this, we replotted the experimentally characterized beam evolution as functions of the propagation direction in the z-axis and the vertical direction in the y-axis by projecting the beam data along the x-axis. Figure 7(a) shows the experimental beam intensity map of the metalens device in the yz-plane (side-view). The solid black box area is zoomed in Fig. 7(b). The white dashed lines indicate the chip facet at $z = 100$ μm. The out-coupled beam remains collimated, achieving a beam waist in the y-direction of $w_0 \approx 3.42$ μm without exhibiting significant divergence within the range of beam focusing. In chip-scale in-plane beam conversion, divergence in the vertical

Optics EXPRESS

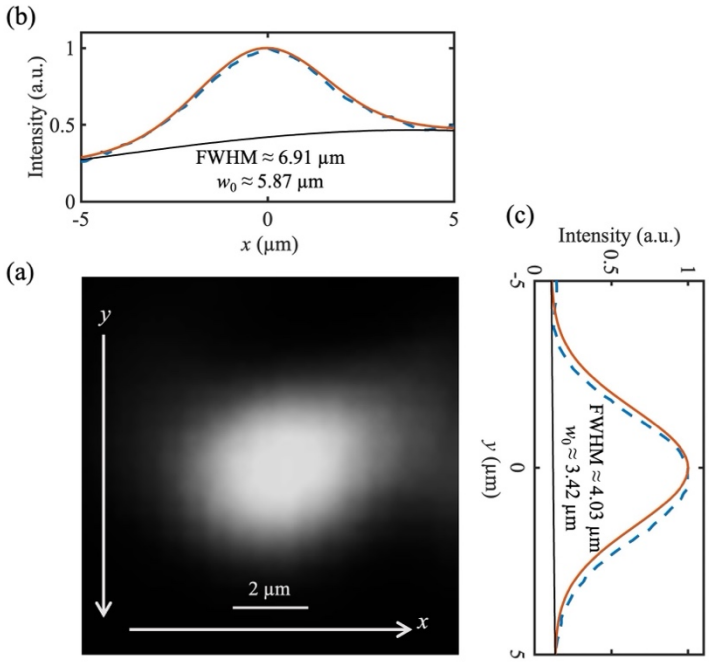

Fig. 6. (a) Zoomed-in microscopic image of the experimental in-plane beam spot at the focal position. (b, c) Gaussian intensity distributions of the beam focal spot along the x- and y-axes, respectively. The dashed blue lines represent the experimental data, while the solid orange lines represent the fitted Gaussian curves. The thin black solid line is a background fitting curve. The full width at half maximum (FWHM) and beam waist w_0 values along both axes are included in the intensity distribution plots, quantifying the beam spot size at the focal position.

direction would often be the limiting factor. However, in our device, which focuses the beam at ≈ 90 μm away from the chip facet, this issue can be mitigated by expanding the out-coupled beam size with SWGs. If the beam was not expanded, the divergence would result in additional power loss and complicate alignment when interfacing with other integrated photonic components. By expanding the beam size in the y-direction using SWGs, we ensure that the beam remains collimated over a sufficient distance, facilitating efficient coupling and integration with other photonic devices.

In our metalens design, the focal distance can be engineered by varying the chip facet width parameter w_{b2}. To demonstrate this, we duplicated the previous simulation and experiment while varying $w_{b2} = 4$, 6, 8, and 10 μm for two different beam conversion lengths, $L_z = 100$ and 150 μm. The size of the slab input, i.e., the length along the x-axis, is fixed at $L_x = 220$ μm. Figure 8 summarizes these results, characterizing the focal distance f_d in each case. The blue and orange colors represent $L_z = 100$ μm and 150 μm, respectively, while the blue circles and orange crosses are the experimentally characterized results. The blue and orange solid lines are the corresponding FDTD simulation results.

As expected, reducing w_{b2} decreases the focal distance f_d since the beam conversion rate in the SWG metalens determines the wavevector of the out-coupled beam and, consequently, the numerical aperture of the metalens. For the conversion length, increasing the beam conversion length L_z brings f_d closer to the chip facet, which might be due to smoother and more efficient beam conversion over a longer distance. We observed these trends in both simulation and

Optics EXPRESS

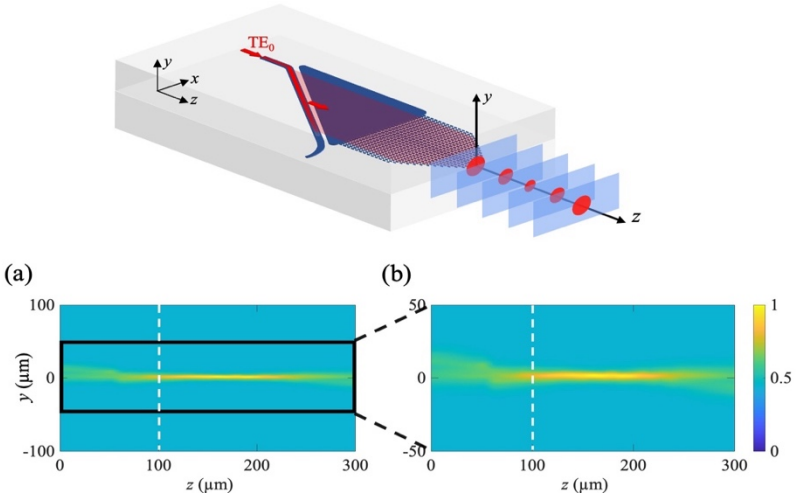

Fig. 7. (a) Experimental intensity map (side-view) of the metalens device with parameters $L_z = 100$ μm, $L_x = 220$ μm and $w_{b2} = 10$ μm. The map shows that the beam is generated in-plane and remains well-collimated along the y-axis after exiting the chip facet at $z = 100$ μm. (b) Zoomed-in image of the same metalens device, highlighting the beam propagation without significant diffraction in the yz-plane. The black solid box indicates the zoomed-in portion of the map plot, while the white dashed line represents the facet of the metalens.

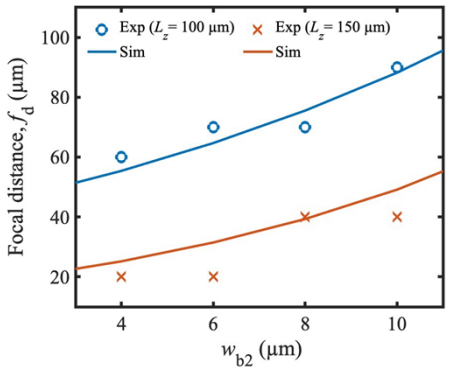

Fig. 8. Simulated and experimentally characterized focal distances as a function of the chip facet width parameter w_{b2} for metalens devices with different z-direction lengths $L_z = 100$ μm and 150 μm. The length of the metalens along the x-axis is fixed at $L_x = 220$ μm. The blue line represents the simulation trend, and the blue circles indicate the experimental data for $L_z = 100$ μm. The orange line represents the simulation trend, and the orange crosses indicate the experimental data for $L_z = 150$ μm. The focal distance f_d decreases with reducing w_{b2} and increasing L_z, demonstrating the tunability of the metalens focal position.

Optics EXPRESS

experimental results, which match reasonably well with some uncertainty in the experiment caused during the imaging processes. The agreement between the simulated and experimental data validates our metalens design approach and demonstrates the ability to control the focal distance by adjusting the chip facet width parameter w_{b2} and the beam conversion length L_z. This tunability allows for the optimization of the metalens performance and its adaptation to specific application requirements, such as focusing the beam at a desired distance from the chip facet or achieving a particular numerical aperture. While previous studies on spot size converters have primarily focused on beam conversion within a chip, mostly between waveguide and slab modes [58–61], our device is uniquely designed to generate a free-space beam that focuses the out-coupled beam far from the chip facet. This enables our device to achieve a significantly long focal distance, approximately 90 µm away from the chip, making it ideal for applications such as optical trapping and particle manipulation. Our device operates in the visible wavelength regime, whereas all previous works have been implemented in the near- or mid-infrared regimes.

4. Conclusion

In this work, we proposed and experimentally demonstrated in-plane out-coupled beam focusing using a silicon nitride photonic subwavelength grating (SWG) metalens at visible wavelength. We utilized a slab mode expander to form a Gaussian intensity beam with a flat wavefront in the slab. Subsequently, the SWG arrays were distributed to manipulate the beam wavefront and converge the in-plane beam after exiting the chip. The experimental characterization and analysis of the out-coupled beam confirmed the generation of an in-plane Bessel-Gaussian-like beam with an extended depth of focus. Our SWG metalens achieves a relatively large-scale modal size transformation, resulting in a large numerical aperture. The beam waist of the input 1D Gaussian slab mode, initially $w_0 = 100$ µm, was focused down to $w_0 \approx 5.87$ µm at a distance of ≈ 90 µm from the chip facet. The out-coupled beam exhibited no significant divergence along the chip's vertical direction, supported by the expanded beam via the SWGs. The focal distance of the metalens device can be tuned by adjusting the SWG metalens parameters, such as the device length L_z and the lens facet width parameter w_{b2}, which determine the SWG array distribution. The distributions of the SWG metalens can be further optimized to achieve a diffraction-limited design and to accommodate other applications [62,63]. The lateral shift of the slab mode beam can be corrected by optimizing the modal expander gap profiles, taking fabrication imperfections into account. Our device is monolithic and highly compatible with CMOS processes, making it readily integrate with other integrated photonic components. Importantly, our in-plane beam-focusing component could facilitate hybrid integration, simplifying the interfacing of photonic chips with other physical domains and unlocking new possibilities for advancing chip-scale applications. The ability to control and manipulate light on-chip, coupled with the potential for hybrid integration, paves the way for novel applications in various fields, such as sensing, imaging, and quantum technologies. Future work could explore the integration of this metalens design with other photonic devices and systems, as well as its adaptation to different wavelength ranges and material platforms.

Funding. Institute for Information and Communications Technology Promotion (RS-2023-00223497); National Research Foundation of Korea (RS-2023-00210997); National Science Foundation (2144568).

Disclosures. The authors declare no conflicts of interest.

Data Availability. Data underlying the results presented in this paper are not publicly available at this time but may be obtained from the authors upon reasonable request.

Optics EXPRESS

References

1. D. J. Moss, R. Morandotti, A. L. Gaeta, *et al.*, "New CMOS-compatible platforms based on silicon nitride and Hydex for nonlinear optics," Nat. Photonics **7**(8), 597–607 (2013).
2. J. Liu, G. Huang, R. N. Wang, *et al.*, "High-yield, wafer-scale fabrication of ultralow-loss, dispersion-engineered silicon nitride photonic circuits," Nat. Commun. **12**(1), 2236 (2021).
3. J. Kitching, E. A. Donley, S. Knappe, *et al.*, "NIST on a Chip: Realizing SI units with microfabricated alkali vapour cells," J. Phys.: Conf. Ser. **723**, 012056 (2016).
4. M. T. Hummon, S. Kang, D. G. Bopp, *et al.*, "Photonic chip for laser stabilization to an atomic vapor with 10−11 instability," Optica **5**(4), 443 (2018).
5. D. Bopp, S. Kang, M. Hummon, *et al.*, Nanophotonic integration of atomic wavelength references, in *Conference on Lasers and Electro-Optics* (OSA, 2019).
6. N. Chauhan, J. Wang, D. Bose, *et al.*, "Ultra-low loss visible light waveguides for integrated atomic, molecular, and quantum photonics," Opt. Express **30**(5), 6960–6969 (2022).
7. A. W. Elshaari, W. Pernice, K. Srinivasan, *et al.*, "Hybrid integrated quantum photonic circuits," Nat. Photonics **14**(5), 285–298 (2020).
8. J. Wang, F. Sciarrino, A. Laing, *et al.*, "Integrated photonic quantum technologies," Nat. Photonics **14**(5), 273–284 (2020).
9. S. Kim, K. Han, C. Wang, *et al.*, "Dispersion engineering and frequency comb generation in thin silicon nitride concentric microresonators," Nat. Commun. **8**(1), 1 (2017).
10. T. J. Kippenberg, R. Holzwarth, and S. A. Diddams, "Microresonator-based optical frequency combs," Science **332**(6029), 555–559 (2011).
11. F. Liang, N. Clarke, P. Patel, *et al.*, "Scalable photonic crystal chips for high sensitivity protein detection," Opt. Express **21**(26), 32306–32312 (2013).
12. S. Lin and K. B. Crozier, "Trapping-assisted sensing of particles and proteins using on-chip optical microcavities," ACS Nano **7**(2), 1725–1730 (2013).
13. X. Fan and I. M. White, "Optofluidic microsystems for chemical and biological analysis," Nat. Photonics **5**(10), 591–597 (2011).
14. E. K. Sackmann, A. L. Fulton, and D. J. Beebe, "The present and future role of microfluidics in biomedical research," Nature **507**(7491), 181–189 (2014).
15. X. Lai, B. Lu, P. Zhang, *et al.*, "Sticker microfluidics: A method for fabrication of customized monolithic microfluidics," ACS Biomater. Sci. Eng. **5**(12), 6801–6810 (2019).
16. K. Ren, J. Zhou, and H. Wu, "Materials for microfluidic chip fabrication," Acc. Chem. Res. **46**(11), 2396–2406 (2013).
17. G. M. Whitesides, "The origins and the future of microfluidics," Nature **442**(7101), 368–373 (2006).
18. P. Pattanayak, S. K. Singh, M. Gulati, *et al.*, "Microfluidic chips: recent advances, critical strategies in design, applications and future perspectives," Microfluid. Nanofluid. **25**(12), 99 (2021).
19. B.-S. Lin, Y.-C. Yang, C.-Y. Ho, *et al.*, "A PDMS-based cylindrical hybrid lens for enhanced fluorescence detection in microfluidic systems," Sensors **14**(2), 2967–2980 (2014).
20. W. C. Griffith, S. Knappe, and J. Kitching, "Femtotesla atomic magnetometry in a microfabricated vapor cell," Opt. Express **18**(26), 27167–27172 (2010).
21. J. A. Sedlacek, A. Schwettmann, H. Kübler, *et al.*, "Microwave electrometry with Rydberg atoms in a vapour cell using bright atomic resonances," Nat. Phys **8**(11), 819–824 (2012).
22. J. M. Pate, J. Kitching, and M. T. Hummon, "Microfabricated strontium atomic vapor cells," Opt. Lett. **48**(2), 383–386 (2023).
23. S. Knappe, V. Shah, P. D. D. Schwindt, *et al.*, "A microfabricated atomic clock," Appl. Phys. Lett. **85**(9), 1460–1462 (2004).
24. M. Yu, Y. Chen, Y. Wang, *et al.*, "Microfabricated atomic vapor cells with multi-optical channels based on an innovative inner-sidewall molding process," Engineering (2023).
25. S. Kim, D. A. Westly, B. J. Roxworthy, *et al.*, "Photonic waveguide to free-space Gaussian beam extreme mode converter," Light: Sci. Appl. **7**(1), 72 (2018).
26. A. Ashkin, J. M. Dziedzic, J. E. Bjorkholm, *et al.*, "Observation of a single-beam gradient force optical trap for dielectric particles," Opt. Lett. **11**(5), 288 (1986).
27. A. Ashkin, J. M. Dziedzic, and T. Yamane, "Optical trapping and manipulation of single cells using infrared laser beams," Nature **330**(6150), 769–771 (1987).
28. A. Ashkin, "History of optical trapping and manipulation of small-neutral particle, atoms, and molecules," IEEE J. Sel. Top. Quantum Electron **6**(6), 841–856 (2000).
29. C. Hosokawa, T. Tsuji, T. Kishimoto, *et al.*, "Convection dynamics forced by optical trapping with a focused laser beam," J. Phys. Chem. C **124**(15), 8323–8333 (2020).
30. S. Yu, J. Lu, V. Ginis, *et al.*, "On-chip optical tweezers based on freeform optics," Optica **8**(3), 409 (2021).
31. F. Merenda, J. Rohner, J.-M. Fournier, *et al.*, "Miniaturized high-NA focusing-mirror multiple optical tweezers," Opt. Express **15**(10), 6075–6086 (2007).
32. C. H. Sow, A. A. Bettiol, Y. Y. G. Lee, *et al.*, "Multiple-spot optical tweezers created with microlens arrays fabricated by proton beam writing," Appl. Phys. B **78**(6), 705–709 (2004).

Optics EXPRESS

33. G. Tkachenko, D. Stellinga, A. Ruskuc, *et al.*, "Optical trapping with planar silicon metalenses," Opt. Lett. **43**(14), 3224 (2018).
34. S. Suwannasopon, F. Meyer, C. Schlickriede, *et al.*, "Miniaturized metalens based optical tweezers on liquid crystal droplets for lab-on-a-chip optical motors," Crystals **9**(10), 515 (2019).
35. R. Geromel, R. Rennerich, T. Zentgraf, *et al.*, "Geometric-phase metalens to be used for tunable optical tweezers in microfluidics," Liq. Cryst. **50**(7-10), 1193–1203 (2023).
36. G. Testa, G. Persichetti, and R. Bernini, "Liquid core ARROW waveguides: A promising photonic structure for integrated optofluidic microsensors," Micromachines **7**(3), 47 (2016).
37. K. D. Leake, B. S. Phillips, T. D. Yuzvinsky, *et al.*, "Optical particle sorting on an optofluidic chip," Opt. Express **21**(26), 32605–32610 (2013).
38. S. Kühn, P. Measor, E. J. Lunt, *et al.*, "Loss-based optical trap for on-chip particle analysis," Lab Chip **9**(15), 2212–2216 (2009).
39. H. Cai, J. W. Parks, T. A. Wall, *et al.*, "Optofluidic analysis system for amplification-free, direct detection of Ebola infection," Sci. Rep **5**(1), 14494 (2015).
40. B. S. Schmidt, A. H. Yang, D. Erickson, *et al.*, "Optofluidic trapping and transport on solid core waveguides within a microfluidic device," Opt. Express **15**(22), 14322–14334 (2007).
41. A. Nitkowski, A. Gondarenko, and M. Lipson, "On-chip supercontinuum optical trapping and resonance excitation of microspheres," Opt. Lett. **35**(10), 1626–1628 (2010).
42. B. S. Ahluwalia, P. McCourt, T. Huser, *et al.*, "Optical trapping and propulsion of red blood cells on waveguide surfaces," Opt. Express **18**(20), 21053–21061 (2010).
43. C. Pin, J.-B. Jager, M. Tardif, *et al.*, "Optical tweezing using tunable optical lattices along a few-mode silicon waveguide," Lab Chip **18**(12), 1750–1757 (2018).
44. Y. Shi, K. T. Nguyen, L. K. Chin, *et al.*, "Trapping and detection of single viruses in an optofluidic chip," ACS Sens. **6**(9), 3445–3450 (2021).
45. S. Gaugiran, S. Gétin, J. Fedeli, *et al.*, "Optical manipulation of microparticles and cells on silicon nitride waveguides," Opt. Express **13**(18), 6956–6963 (2005).
46. D. Jeon, K. Shin, S.-W. Moon, *et al.*, "Recent advancements of metalenses for functional imaging," Nano Converg **10**(1), 24 (2023).
47. C. Xiang, W. Jin, and J. E. Bowers, "Silicon nitride passive and active photonic integrated circuits: trends and prospects," Photonics Res. **10**(6), A82 (2022).
48. J. Lee, J.-H. Lee, and S. Kim, "Integrated photonic in-plane beam converter for Bessel-Gaussian beam generation," in *The 25th European Conference on Integrated Optics* (Springer Nature Switzerland, 2024), pp. 540–544.
49. G. W. Milton, *The Theory of Composites 1st Edn* (Cambridge University Press, 2002).
50. S. Jahani, S. Kim, J. Atkinson, *et al.*, "Controlling evanescent waves using silicon photonic all-dielectric metamaterials for dense integration," Nat. Commun **9**(1), 1893 (2018).
51. M. B. Mia, S. Z. Ahmed, I. Ahmed, *et al.*, "Exceptional coupling in photonic anisotropic metamaterials for extremely low waveguide crosstalk," Optica **7**(8), 881 (2020).
52. M. B. Mia, S. Z. Ahmed, N. Jaidye, *et al.*, "Mode-evolution-based ultra-broadband polarization beam splitter using adiabatically tapered extreme skin-depth waveguide," Opt. Lett. **46**(18), 4490–4493 (2021).
53. S. Z. Ahmed, I. Ahmed, M. B. Mia, *et al.*, "Ultra-high extinction ratio polarization beam splitter with extreme skin-depth waveguide," Opt. Lett. **46**(9), 2164–2167 (2021).
54. M. B. Mia, N. Jaidye, I. Ahmed, *et al.*, "Broadband integrated polarization splitter and rotator using subwavelength grating claddings," Opt. Express **31**(3), 4140–4151 (2023).
55. I. Ahmed, S. Z. Ahmed, N. Jaidye, *et al.*, "High-density integrated delay line using extreme skin-depth subwavelength grating waveguides," Opt. Lett. **48**(7), 1662 (2023).
56. M. F. Kabir, M. B. Mia, I. Ahmed, *et al.*, "Anisotropic leaky-like perturbation with subwavelength gratings enables zero crosstalk," Light: Sci. Appl **12**(1), 135 (2023).
57. D. Pimbi, M. B. Mia, N. Jaidye, *et al.*, "Integrated polarization-free Bragg filters with subwavelength gratings for photonic sensing," Opt. Express **32**(2), 2147 (2024).
58. Y. Zhang, Y. He, H. Wang, *et al.*, "Ultra-broadband mode size converter using on-chip metamaterial-based Luneburg lens," ACS Photonics **8**(1), 202–208 (2021).
59. J. M. Luque-González, R. Halir, J. G. Wangüemert-Pérez, *et al.*, "An ultracompact GRIN-lens-based spot size converter using subwavelength grating metamaterials," Laser Photon. Rev **13**(11), 1900172 (2019).
60. Z. Wang, T. Li, A. Soman, *et al.*, "On-chip wavefront shaping with dielectric metasurface," Nat. Commun **10**(1), 3547 (2019).
61. Z. Ren, B. Dong, Q. Qiao, *et al.*, "Subwavelength on-chip light focusing with bigradient all-dielectric metamaterials for dense photonic integration," InfoMat **4**(2), 1 (2022).
62. S. H. Badri, M. M. Gilarlue, and H. Taghipour-Farshi, "Rectangular Maxwell's fisheye lens via transformation optics as a crossing medium for dissimilar waveguides," J. Opt. Soc. Am. B **37**(8), 2437 (2020).
63. S. Hadi Badri and M. M. Gilarlue, "Low-index-contrast waveguide bend based on truncated Eaton lens implemented by graded photonic crystals," J. Opt. Soc. Am. B **36**(5), 1288 (2019).